Tomographic filtering of high-resolution mantle circulation models: Can seismic heterogeneity be explained by temperature alone?

B. S. A. Schuberth[1], H.-P. Bunge[1], J. Ritsema[2]

Bernhard Schuberth, Department of Earth and Environmental Sciences, Ludwig-Maximilians-Universität München, Theresienstr. 41, 80333 Munich, Germany. (mail@bernhard-schuberth.de)

[1]Department of Earth and Environmental

Sciences, Ludwig-Maximilians-Universität

München, Germany

[2]Department of Geological Sciences,

University of Michigan, USA

D R A F T   March 25, 2009, 2:05pm   D R A F T

Abstract.

Recent high-resolution mantle circulation models (MCMs) together with thermodynamic mineralogical models make it possible to construct 3-D elastic mantle heterogeneity based on geodynamic considerations. In the presence of a strong thermal gradient across D″ and corresponding large temperature variations in the lower mantle, the heterogeneity predicted from isochemical whole mantle flow agrees well with tomographic models in terms of magnitudes of S-wave velocity (v_s) variations [*Schuberth et al.*, 2009]. Here, we extend the comparison of geodynamic and tomographic structures by accounting explicitly for the limited resolving power of tomography. We focus on lateral variations in v_s and use the resolution operator $\mathcal{R}$ associated with S20RTS [*Ritsema et al.*, 2004] to modify our geodynamic models so that they reflect the long-wavelength (>1000 km) nature and the effects of heterogeneous data coverage and damping inherent to the tomographic inversion. Prior to the multiplication with $\mathcal{R}$, the geodynamic models need to be reparameterized onto the basis of S20RTS. The magnitude reduction introduced by this reparameterization is significant and needs careful assessment. We attempt a correction of the reparameterization effects and find that the inherent tomographic filtering alone then leads to a magnitude reduction by a factor of $\sim$2 in the lower mantle. Our tomographically filtered models with strong core heating agree well with S20RTS, which resolves maximum negative anomalies of around -1.5% in the lowermost mantle. Temperature variations on the order of +1000 K, corresponding to perturbations of around -3% in v_s

in the unfiltered model, would be seen as -1.5% when "imaged" with the data and damping of S20RTS. This supports our earlier finding that isochemical whole mantle flow with strong core heating and a pyrolite composition can be reconciled with tomography. In particular, the large lateral temperature variations associated with lower mantle plumes are able to account for the slow seismic anomalies in the large low velocity zones under Africa and the Pacific. We also find that strong gradients in shear wave velocity of 2.25% per 50 km in our unfiltered models compare well with the sharp sides of the African superplume [e.g., *Ritsema et al.*, 1998; *Ni et al.*, 2002].

1. Introduction

Seismologists now widely agree that the large scale structure of the lower mantle is dominated by a ring of seismically fast material in the circum-Pacific region and by two prominent slow anomalies under Africa and the Pacific [e.g., *Dziewonski et al.*, 1977; *Su et al.*, 1994; *Li and Romanowicz*, 1996; *Grand et al.*, 1997; *van der Hilst et al.*, 1997; *Su and Dziewonski*, 1997; *Kennett et al.*, 1998; *Masters et al.*, 2000; *Ritsema et al.*, 2004; *Montelli et al.*, 2006; *Panning and Romanowicz*, 2006; *Simmons et al.*, 2007; *Houser et al.*, 2008; *Kustowski et al.*, 2008]. While the fast seismic structures can generally be related to the history of plate subduction [*Richards and Engebretson*, 1992; *Bunge et al.*, 1998; *Lithgow-Bertelloni and Richards*, 1998; *Becker and O'Connell*, 2001; *Conrad and Lithgow-Bertelloni*, 2002; *McNamara et al.*, 2002] the nature of the large low velocity zones remains elusive.

It has been proposed that these "superplumes" are chemically distinct from the surrounding material as they show anticorrelated variations in shear and bulk sound velocity as well as evidence for an increased density [*van der Hilst and Karason*, 1999; *Ritsema and van Heijst*, 2002; *Masters et al.*, 2000; *Ishii and Tromp*, 2001; *Wen et al.*, 2001; *Ni et al.*, 2002; *Trampert et al.*, 2004; *Wang and Wen*, 2004]. The large amplitudes of lateral variations in shear wave velocity of up to -3 to -4% ,in particular, have been taken to argue for compositional heterogeneity [e.g., *Farnetani and Samuel*, 2005; *Samuel et al.*, 2005].

Recently, we have shown that strong seismic heterogeneity in the lowermost mantle can be reconciled with isochemical whole mantle flow in the presence of a large thermal

gradient across D″ on the order of 1000–1500 K [*Schuberth et al.*, 2009]. The strong thermal gradient in the lower boundary layer of our mantle circulation models leads to high excess temperatures of lower mantle upwellings with similar magnitude of +1000–1500 K. These correspond to significant negative S-wave anomalies of around −3 to −4% after conversion to seismic heterogeneity with thermodynamically self-consistent models of mantle mineralogy [*Piazzoni et al.*, 2007; *Stixrude and Lithgow-Bertelloni*, 2005, 2007]. The strong reduction in shear wave velocity in our models compares well with the negative v_s anomalies mapped by recent tomographic studies in the large low velocity zones under Africa and the Pacific [*Montelli et al.*, 2006; *Simmons et al.*, 2007; *Houser et al.*, 2008]. We note that a high CMB temperature and a correspondingly large temperature drop across D″, with associated high heat flow, is consistent with a number of studies from geodynamics, seismology and mineral physics [e.g., *Glatzmaier and Roberts*, 1995; *Kuang and Bloxham*, 1997; *Boehler*, 2000; *Steinle-Neumann et al.*, 2001; *Buffett*, 2002; *Gubbins et al.*, 2004; *Nimmo et al.*, 2004; *Nolet et al.*, 2006; *Alfè et al.*, 2002; *Alfè et al.*, 2007; *van der Hilst et al.*, 2007; *Steinberger and Holme*, 2008].

In *Schuberth et al.* [2009], we did not account for the limited resolving power of tomography, which is known to be important in the analysis of geodynamic models. For example, *Mégnin et al.* [1997] applied the "linear tomographic filter", corresponding to model SAW12D [*Li and Romanowicz*, 1995] to mantle convection models. They showed that seismic data coverage significantly affects the spectral characteristics of their geodynamic models. *Bunge and Davies* [2001] traced rays through mantle circulation models, and found a significant change in the pattern of heterogeneity in regions of poor ray-coverage. Using the same approach, *Davies and Bunge* [2001] observed a systematic bias towards

negative synthetic traveltime residuals and explained this by most earthquakes being located in areas of fast seismic velocities (i.e., active subduction). Recently, *Ritsema et al.* [2007] applied the resolution operator corresponding to the tomographic model S20RTS to isochemical and thermochemical models of mantle circulation and observed a substantial decrease in the total spectral power of heterogeneity and a change in geographic pattern.

The aforementioned studies clearly demonstrate the need to account for the limited resolving power of tomography. However, being based on simple depth-independent linear conversions between temperature and seismic velocities, the studies were limited in their ability to investigate the effects of tomographic resolution on the magnitudes of velocity anomalies. As noted before, our models benefit from recent progress in mineral physics, which now provides improved relations between thermal and elastic parameters based on the thermodynamically self-consistent treatment of mineral phase assemblages. By combining these advances with an analysis of the effects of limited tomographic resolution, a quantitative comparison of geodynamically predicted seismic heterogeneity with tomography can be attempted. In the present study, we therefore extend the assessment of our MCMs by "filtering" their shear wave velocity structures with the resolution operator of S20RTS.

We start this paper with a short description of the tomographic filtering process. This involves the transformation of our geodynamic models onto the parameterization of S20RTS, which has important implications for the following analysis of seismic heterogeneity. In the comparison of our tomographically filtered models with S20RTS we focus on statistical measures such as the spectral power, histograms and root-mean-square (RMS) profiles of heterogeneity.

The characteristics of our filtered models agree well with S20RTS. As expected, the magnitudes of seismic heterogeneity are significantly reduced during the filtering process. The amplitude reduction is due, in part, to the reparameterization and we explore possibilities to correct for this effect in a second step. Importantly, our MCM with strong core heating shows negative v_s anomalies of around -1.5 to -2% in the lowermost mantle when only the effects of uneven data coverage and damping are considered. These values are fully compatible with the anomalies mapped by S20RTS. Finally, we note that the gradients of seismic heterogeneity in the original (unfiltered) version of this model compare well with those inferred from direct observations of traveltimes sampling the lower mantle under Africa [*Ritsema et al.*, 1998; *Ni et al.*, 2002].

2. Parameterization of Models and Tomographic Filtering

2.1. Tomographic Model S20RTS

S20RTS is a model of isotropic shear velocity perturbations from the (anisotropic) 1-D model PREM. The model is based on three different data types: normal mode splitting functions, Rayleigh wave phase velocities and body wave travel times [*Ritsema et al.*, 2004]. It is parameterized laterally in spherical harmonics up to degree 20 and radially with 21 spline functions. The radial splines interpolate continuously across the 660 km discontinuity and their spacing is denser in the upper mantle where the resolving power of the data is higher. In total, S20RTS includes ~10,000 parameters resulting in a lateral resolution of around 1000 km. After damping, about 3000 effective unknowns are resolved. In the inversion, it is assumed that P velocity anomalies are related to S velocity anomalies throughout the mantle by $\partial \ln v_p = 0.5 \cdot \partial \ln v_s$, a scaling based on globally recorded P and

S wave traveltime residuals [*Robertson and Woodhouse*, 1995; *Ritsema and van Heijst*, 2001].

2.2. Mantle Circulation Models

We construct seismic mantle heterogeneity by post-processing the present day temperature field obtained from mantle circulation models with one of the aforementioned thermodynamic mineralogical models, which includes all the effects of phase changes in a 5-oxide (CFMAS) pyrolitic composition [*Stixrude and Lithgow-Bertelloni*, 2005, 2007]. Apart from the isochemical, pyrolitic nature of the investigated models, two basic assumptions are made in the prediction of global mantle heterogeneity: 1) a large-scale flow structure related to past plate motion, 2) a radial viscosity profile that agrees with postglacial rebound and geoid observations. Details on the modeling and the characteristics of predicted v_s heterogeneity can be found in *Schuberth et al.* [2009]. We note, that the flow calculations currently do not incorporate the dynamic effects of phase transformations. Furthermore, anelastic effects and the post-perovskite phase are not included in the mineralogical model. In the following, we summarize the numerical parameterization of our MCMs, which is important in the context of tomographic filtering.

The MCMs are computed with the code TERRA [*Bunge and Richards*, 1996; *Bunge et al.*, 1996, 1997] and are discretized with a mesh derived from the regular icosahedron, which provides almost equidistant grid spacing throughout the mantle. Horizontal grid spacing is around 30 km at the Earth's surface and due to the sphericity of the model about 15 km at the CMB. In radial direction, the model is discretized with 128 equidistant layers leading to ∼25 km vertical grid spacing. This fine discretization leads to a total of around 80 million grid points, which allows us to simulate large scale mantle flow with

Earth-like convective vigor and to employ a thermal Rayleigh number of $\sim 10^9$ based on internal heating. Thus, we are able to resolve a characteristic thermal boundary layer thickness on the order of 100 km, comparable to that of oceanic lithosphere. The high-resolution mantle circulation models are implemented on 128 cores of a topical compute cluster dedicated to large-scale geophysical modeling [*Oeser et al.*, 2006].

We focus our analysis of tomographic filtering effects on two of the four models described in *Schuberth et al.* [2009], namely M1 and M2. The models have the same viscosity stratification, but are end-member models in terms of bottom heating. The reference viscosity of the upper mantle is 1×10^{21} Pa s, while the viscosity in both the lithosphere and the lower mantle is 100 times larger. Model M1 is heated mainly from within (5% core heating), whereas model M2 has a strong component of bottom heating of around 35% of the surface heat flux. We note that in our study the term "lithosphere" is used only to denote the uppermost layer of our viscosity profile. As we do not account for the existence of chemical variations in the upper 100-150 km, we will not attempt a comparison of our models with tomography in this depth range.

2.3. Tomographic Filtering

We modify our theoretically predicted mantle heterogeneity using the resolution operator $\mathcal{R} = \mathbf{G}^\dagger \mathbf{G}$ associated with S20RTS, where $\mathbf{G}$ is the operator of the seismic forward problem and $\mathbf{G}^\dagger$ its generalized inverse. Details of this procedure can be found in *Ritsema et al.* [2007]. The geodynamic prediction of seismic heterogeneity is defined as the "true" model $\mathbf{m}$, which is multiplied with $\mathcal{R}$ to obtain a "filtered" representation $\mathbf{m}'$ as if imaged by tomographic inversion:

$$\mathbf{m}' = \mathcal{R} \cdot \mathbf{m} \qquad\qquad (1)$$

Since $\mathcal{R}$ includes all the effects on resolution due to limited data coverage and model regularization, this process is computationally easier and faster than ray tracing and inversion of synthetic traveltimes in case $\mathcal{R}$ is explicitly available. The filtered geodynamic model can then be compared to the corresponding tomographic model. In this respect, it is important that the resolution operator $\mathcal{R}$ is computed based on the same damping parameter ϵ as the tomographic model. In the case of S20RTS, ϵ was chosen to be 0.035 [*Ritsema et al.*, 2007], which we therefore adopt here as well.

Theoretical predictions of mantle heterogeneity are usually taken from numerical simulations. As noted before, these are performed on grids with a large number of nodes to accommodate the vigorous convective regime of the Earth. Grid spacings have to be on the order of several tens of kilometers globally. This typically results in meshes with $\sim 10^7$ degrees of freedom [e.g., *Bunge et al.*, 2002; *McNamara and Zhong*, 2004]. In contrast, global tomographic models currently provide a maximum spatial resolution on the order of several hundred to thousand kilometers [*Ritsema et al.*, 2004; *Montelli et al.*, 2006; *Simmons et al.*, 2007; *Houser et al.*, 2008]. Geodynamic mantle structures thus have to be reparameterized onto the basis of the specific tomographic model being compared with, as resolution matrices are given in the corresponding parameterizations.

In our case, the reparameterization is carried out by expanding $v_s(\theta, \phi)$ from our MCMs into the parameterization of S20RTS:

$$v_s(\theta, \phi) = \sum_{k=1}^{21} \sum_{l=0}^{20} \sum_{m=-l}^{+l} a_{klm}\, F_k(r)\, Y_{lm}(\theta, \phi)\,. \tag{2}$$

Here, $F_k(r)$ are the radial spline functions and $Y_{lm}(\theta, \phi)$ the spherical harmonics of degree l and order m. The coefficients a_{klm} are determined by least-squares fitting. We note that aliasing effects due to the expansion over a finite sum of global basis functions are in the case of our MCMs around 8 orders of magnitude smaller than the actual signal.

Then, the parameters of the adapted model, which defines the true structure **m** in Equation (1), can be tomographically filtered by multiplication with $\mathcal{R}$. The reparameterization leads to a drastic reduction in the model dimensionality, which in turn results in a significant alteration of the model characteristics, as will be shown in section 3. We introduce the following notation for our MCMs: M^o denotes their original parameterization, M^r the reparameterization to the basis of S20RTS, and M^f denotes the reparameterized and filtered model (i.e., M^r multiplied with $\mathcal{R}$). Changes in characteristics between the original model M^o and M^f are thus a combination of two separate effects. In the following, we use the terms "tomographic filtering" or "resolving power of tomography" only for the modification of models due to the multiplication with the resolution matrix.

3. Results

3.1. Effects of Parameterization and Tomographic Filtering

Figure 1 shows the shear wave velocity structure of model M2 in the two parameterizations, and filtered to the resolution of S20RTS. In Figure 1a, M2 is plotted in its original parameterization on the numerical grid of the code TERRA (i.e., $M2^o$). The earth-like convective vigor leads to a narrow upper thermal boundary layer, around 100 km thick. Thin and elongated fast velocity structures at 340 km depth (e.g., all around the Pacific)

correspond to cold, downwelling slabs located in regions of present day subduction. With increasing depth, their locations change according to earlier stages of subduction as given by the plate motion history. In the lowermost mantle, the downwelling material spreads laterally above the CMB and the strong lower thermal boundary layer leads to significant hot upwellings, as for example in the southeast Pacific.

In Figure 1b, M2 is plotted in the parameterization of S20RTS (i.e., $M2^r$). Spatial resolution is significantly lower than in $M2^o$ due to the restriction of model parameters to spherical harmonic degrees lower than 20. The reparameterization results in the spreading of anomalies and in a reduction of their amplitudes. Especially the thin slabs in the upper mantle are substantially broadened compared to the original parameterization. At 100 km depth, fast continental areas as well as slow mid-ocean ridge systems display lower values than in the original parameterization. The same is true in the lower mantle, where the magnitudes of the large slow anomalies located under the Pacific, Africa and the Indian Ocean are reduced.

Figure 1c shows $M2^f$; that is, $M2^r$ filtered to the resolving power of S20RTS. The main effect of the filtering is to further reduce the amplitudes in the lower mantle, especially at 2800 km depth. There, the shape of the anomalies is not affected much in contrast to the mid-mantle. At 1450 km and 2100 km, some lateral smearing of heterogeneity can be observed. Interesting to note is that in certain regions of the upper mantle amplitudes appear to be enhanced due to vertical smearing of structure from above or below. This is, for example, the case for the slow seismic velocities under the Pacific and the fast velocities corresponding to the Farallon slab under western North America at 340 km depth.

Irrespective of the general magnitude reduction, Figures 1b and 1c indicate that the pattern of seismic heterogeneity in the lowermost mantle is resolved quite well by S20RTS. This is probably related to the fact that the S20RTS data set includes a large number of traveltimes of S waves that have diffracted along the core, in addition to normal mode splitting coefficients [*Ritsema et al.*, 2004], which optimizes the coverage in the lowermost mantle.

For comparison, S20RTS is shown in Figure 1d. The general character of our filtered model M2^f agrees quite well with S20RTS. The poor geographic correlation, however, is primarily due to the unknown initial condition of the forward problem of mantle dynamics [*Bunge et al.*, 2003], and uncertainties in the plate motion history [*Bunge et al.*, 2002; *McNamara and Zhong*, 2005; *Schuberth et al.*, 2009]. Thus, independently of the important effects of tomographic resolution, this limits the use of morphological considerations in the assessment of geodynamic models, unless better constraints, especially on the temperature variations in the past, become available.

3.2. Effects on Spectral Characteristics of Heterogeneity

In Figure 2, we plot spectral heterogeneity maps (SHM) [*Jordan et al.*, 1993], which are contour plots of spectral amplitude of heterogeneity versus depth. Shown are M1 and M2 in their original, reparameterized, and filtered representations (Figs. 2a–c and 2d–f, respectively). In addition, we show corresponding radial profiles of the root-mean-square power of the spherical harmonics expansion. Spectral power σ_l per degree l is computed at each depth level and for spherical harmonic degrees $l = 1, \ldots, 20$ by [*Dahlen and Tromp*, 1998, B.8]

$$\sigma_l = \sqrt{\frac{1}{2l+1}\left[a_{l0}^2 + \sum_{m=1}^{l}(a_{lm}^2 + b_{lm}^2)\right]}, \qquad (3)$$

where a_{lm} and b_{lm} are the coefficients of the expansion and the RMS power $\delta\hat{v}$ up to degree l_{max} is given by:

$$\delta\hat{v}_{l_{max}} = \sqrt{\frac{1}{\sqrt{4\pi}}\sum_{l=1}^{l_{max}}(2l+1)\sigma_l^2}. \qquad (4)$$

The spectral characteristics of both MCMs are quite similar with model M1 only showing less power overall. The strong degree two in the lower mantle is mainly a consequence of the long-wavelength structure of earlier stages of the plate motion history. Together with the viscosity stratification this generally leads to a red spectrum of the mantle [*Bunge and Richards*, 1996; *Bunge et al.*, 1998, 2002].

In the original parameterization of M1 and M2, heterogeneity is strongest in the thermal boundary layers, where it is distributed over a wide range of spatial scales. In the mid-mantle, heterogeneity is weaker and concentrated in low degrees. Thin layers of increased heterogeneity in the upper mantle correspond to phase transformations at 410, 520 and 660 km depth.

Figures 2b and 2e show the SHMs of the reparameterized models M1^r and M2^r. Differences to the original models are small and derive from the difference in radial parameterization. The strong heterogeneity in the transition zone is smeared vertically and the distinct band of the 410 km discontinuity is smoothed away. Heterogeneity in the lowermost mantle is affected as well, which can also be seen from the RMS profiles.

The SHMs of the filtered models $M1^f$ and $M2^f$ are given in Figures 2c and 2f, respectively. Power is mainly reduced in high degrees, and the lowermost mantle is affected stronger than the rest. This is also visible from the RMS profiles. The band of high spectral power in the transition zone, which is more pronounced in $M2^r$, is mostly filtered away and only low degrees (1–5) still show substantial power there.

3.3. Effects on Magnitudes of Heterogeneity

Figure 3 shows histograms of the lateral v_s variations in our MCMs; that is, we contour the distribution of magnitudes of heterogeneity as a function of relative perturbation and depth. In analogy to the SHMs in Figure 2, the histograms are given for the original, reparameterized, and filtered versions of M1 and M2. First, we note that in the original parameterization (Figs. 3a and 3d), largest amplitudes are located in the upper mantle and the transition zone with values of up to 5% and more. In the upper part of the lower mantle, heterogeneity is weaker and the distribution is asymmetric towards fast seismic anomalies (i.e., positive skewness). In M2, the skewness changes with depth being negative in the lowermost mantle as a consequence of the strong thermal gradient across D''. The most prominent feature in the original parameterization of M2 is the asymmetry of maxima in the lowermost mantle with values of -4% and $+2.8\%$. In contrast, M1 with weak core heating only shows small negative anomalies of less than -1% in most of the lower mantle and a positive skewness throughout.

Figures 3b and 3e show the histograms of the reparameterized models $M1^r$ and $M2^r$, and a comparison with Figures 3a and 3d illustrates that the reduction of magnitudes introduced in this step is depth-dependent. Amplitudes of heterogeneity are decreased stronger in the upper half than in the lower half of the mantle. This indicates that the

short-scale variations in the upper mantle are not captured by the degree-20 parameter-ization. Amplitude reduction in the lower mantle is smaller due the predominance of long-wavelength structure there, which in turn is a consequence of the higher viscosity and the absence of major phase changes. Effects on positive and negative anomalies are different as can be seen, for example, from the change in skewness in the lower mantle. The same holds for the transition zone, where positive anomalies are affected stronger than negative perturbations, as is apparent from the fact that the positive anomalies at 660 km depth have all but disappeared.

As expected, the tomographic filtering further reduces the amplitudes of heterogeneity (see Figs. 3c and 3f). Both models show similar magnitudes of positive anomalies in the lower mantle. Similar to the original parameterization, model M1^f displays asymmetric distributions towards positive values in all of the lower mantle, only that maximum neg-ative v_s anomalies are around -0.5% now. The histogram of M2^f is more symmetric and maximum anomalies in the lowermost mantle are around $\pm 1.5\%$ reaching up to $\pm 2\%$ close to the CMB.

3.4. Quantitative Analysis of Reparameterization and Filtering Effects

To quantitatively analyze the effects of reparameterization and tomographic filtering, we first concentrate on root-mean-square amplitudes of heterogeneity. Figure 4a shows RMS profiles for v_s variations in the three versions of M2 (i.e., the original, reparameterized, and filtered model). RMS values in the original parameterization are largest in the upper thermal boundary layer with values exceeding 2%. Between 300 and 1500 km depth, heterogeneity decreases to values of 0.5% and monotonically increases again from this

mid-mantle minimum to values of up to 1.6% near the CMB. Strong variations of RMS in the upper mantle correspond to the phase transformations in the transition zone.

RMS amplitudes of the reparameterized model are lower than in the original parameterization. In addition, only one maximum is left in the transition zone as noted also for the SHMs in section 3.2. Between 800 km and 2000 km depth, RMS values are below 0.5% and reach ~1.2% close to the CMB. The amplitude difference to the original parameterization is strongest in the transition zone and uppermost lower mantle and decreases with depth. As mentioned above, the depth-dependence of this magnitude reduction relates to the different nature of heterogeneity between upper and lower mantle (i.e., short-scale variations in the upper mantle due to a complex set of phase changes, and predominantly long-wavelength features in the lower mantle resulting from the higher viscosity there).

After applying the tomographic filter, the RMS profile is nearly constant in most of the mantle with values close to 0.3%, but still shows a weak minimum at around 1500 km depth. A comparison with the profile of the reparameterized model shows that the reduction of RMS values is stronger in the lower half of the mantle indicating again that the resolving power of S20RTS is better in the upper mantle. There, mainly the local maximum in the transition zone is reduced. In the lowermost 300 km, the filtered model shows a strong increase in RMS values reaching ~0.7% close to the CMB.

Figure 4b shows the total relative amplitude reduction resulting from the filtering procedure. In addition, we plot the separated contributions from the effects of reparameterization and tomographic filtering. The total relative amplitude reduction is almost constant with depth in the lower mantle and exceeds 0.5 nearly everywhere. Close to the CMB, about two-thirds of the original amplitude is lost. Note that the profiles for

the reparameterization and tomographic filtering effects cross at around 1500 km depth. Above this depth, the total reduction is dominated by the reparameterization while the effects of tomographic resolution are stronger below.

3.5. Correcting for the Effects of Reparameterization

As seen from Figures 2–4, the characteristics of the tomographically filtered models are significantly influenced by the effects of the reparameterization. A first order correction of these effects could be attempted in a post-processing step to the tomographic filtering due to the linear nature of $\mathcal{R}$; that is, the heterogeneity of short-scale structure, which is lost in the degree-20 parameterization of the filtering procedure, can be considered as an additional contribution in the quantitative analysis. In the following, we try to do this by correcting for the total amplitude reduction resulting from the reparameterization. This allows estimates of the properties of our models as if only exposed to the limited resolving power of S20RTS. As will be discussed in section 4, the exact extent to which the reparameterization effects have to be accounted for depends on the amount of aliasing of short-scale heterogeneity into the long-wavelength structure of tomographic models. Thus, the correction attempted here provides an upper bound for the magnitudes of the tomographically filtered seismic heterogeneity derived from our MCMs.

The RMS values $\delta\hat{v}^{f+}$ for the tomographic filter effect alone are obtained by computing the ratio of RMS values of the tomographically filtered model M^f with the reparameterized model M^r for each depth d. In this way, we isolate the component of amplitude reduction associated with $\mathcal{R}$. We then multiply this depth-dependent ratio $\frac{\delta\hat{v}^f}{\delta\hat{v}^r}$ with the RMS values of the original model $\delta\hat{v}^o$:

$$\delta\hat{v}^{f+}(d) \;=\; \delta\hat{v}^o(d) \cdot \frac{\delta\hat{v}^f(d)}{\delta\hat{v}^r(d)} \;. \tag{5}$$

In Figure 5, we show RMS profiles for our filtered models corrected in this manner, which we also denote $M1^{f+}$ and $M2^{f+}$. The RMS profile of S20RTS is plotted for comparison. The general characteristics of the original models, such as the large amplitudes close to the thermal boundary layers and peaks in the transition zone, are conserved when only accounting for the tomographic filtering; that is, without the bias due to the reparameterization. As in the original parameterization, model $M2^{f+}$ with high CMB heat flux has larger values than $M1^{f+}$ at all depths. Below 1500 km depth, the difference between $M1^{f+}$ and $M2^{f+}$ increases gradually. RMS values in $M2^{f+}$ get larger below 2500 km, where model $M1^{f+}$ only shows a moderate increase. Directly above the CMB models $M1^{f+}$ and $M2^{f+}$ display RMS amplitudes of 0.4% and 0.8%, respectively. Below 1500 km depth, $M2^{f+}$ agrees remarkably well with S20RTS, while $M1^{f+}$ shows values that are 20–30% lower than S20RTS there.

3.6. Correction of Spectral Characteristics

In a next step, we perform a similar correction as in section 3.5 for the spectral heterogeneity maps. In this case, we account for the loss of spectral power during the reparameterization for each spherical harmonic degree l, separately, again depending on depth d:

$$\sigma_l^{f+}(d) \;=\; \sigma_l^o(d) \cdot \frac{\sigma_l^f(d)}{\sigma_l^r(d)} \tag{6}$$

Figures 6a,b show the SHMs for the filtered and corrected models M1^{f+} and M2^{f+}, respectively. The comparison with Figures 2a and 2d illustrates the now isolated effect of the limited tomographic resolution of S20RTS alone. Heterogeneity is mostly reduced in the high degrees of the lower mantle. Furthermore, the tomographic filtering results in vertical smearing of power from the transition zone into the upper part of the lower mantle.

Except for their magnitudes, the spectral characteristics of M1^{f+} and M2^{f+} are very similar, in analogy to the original SHMs in Figures 2a and 2d. Both show a marked change in spectral pattern across the 660 km discontinuity, which is even more pronounced than in the unfiltered original models due to the strong reduction of power in high degrees of the lower mantle. The characteristic difference between upper and lower mantle compares well with the change in spectral pattern seen in S20RTS (Fig. 6c), and is a consequence of the phase changes in the transition zone together with the unresolved structure in the higher degrees of the lower mantle.

3.7. Correction of Histograms

We also attempt a first order correction of the amplitude distributions in our MCMs. For this, we take the values of seismic heterogeneity from the filtered model and multiply them with the depth-dependent ratio of RMS values from the original model and the reparameterized model (which is similar to the operation in Equation (5)). To account for possible asymmetries in the reparameterization, we perform this operation for positive and negative perturbations separately.

In Figure 7, we show histograms for the filtered and corrected models M1^{f+} and M2^{f+} together with the histogram of S20RTS. The main characteristics of the original models

are conserved (e.g., largest amplitudes in the upper mantle, and in M2^o a change in skewness from positive to negative throughout the lower mantle, which can also be seen in the histogram of S20RTS). Comparing the maximum values in Figures 7a,b with those in Figures 3a,d indicates that amplitudes of heterogeneity in our MCMs are lowered by almost a factor of 2 when affected by the limited tomographic resolution alone. The histogram of M2^{f+} (Fig. 7b) compares well with S20RTS for both positive and negative amplitudes in most depth levels. This is markedly different for M1^{f+}, which shows maximum negative anomalies of less than -0.5% in most of the lower mantle as a consequence of the lower core heating.

4. Discussion

4.1. Lateral Temperature Variations and Magnitudes of Seismic Heterogeneity

An important result of our analysis is the change in the characteristics of our geodynamic models introduced by the reparameterization. The transformation of model parameters from the original high-resolution grid ($\sim$25 km global grid spacing) onto the low-degree spherical harmonics basis of S20RTS is needed to perform the tomographic filtering and results in a significant "loss" of short-scale heterogeneity. The fact that heterogeneity in the upper mantle suffers more drastically from the long-wavelength reparameterization is related to velocity variations being present on very short length-scales there (see SHMs in Figs. 2a and 2d), which in turn is a consequence of the complex set of phase transformations in the transition zone [*Schuberth et al.*, 2009]. Interestingly, the amplitude reduction associated with the reparameterization appears to be not only depth-dependent, but also different for positive and negative velocity variations, as can be seen from the change in skewness of the histograms in Figure 3. Most importantly, however, the amplitude

reduction induced by the reparameterization is comparable in magnitude to the effects of uneven data coverage and damping.

The tomographic filtering is also depth-dependent, indicating a better ability of S20RTS to resolve velocity variations in the upper mantle due to fundamental mode and overtone surface wave constraints. Owing to their different depth dependencies of relative amplitude loss, the combination of reparameterization and subsequent multiplication with $\mathcal{R}$ then leads to an almost constant total magnitude reduction in the lower mantle of around 60 percent of the original amplitudes (see Fig. 4).

The loss of short-scale heterogeneity associated with the reparameterization in itself seems unphysical, as structural variations on length-scales of around 100 km and less are expected to be present in the mantle (e.g., slabs). However, whether the reparameterization should be accounted for in comparisons of geodynamic and seismic models depends on the potential of short-scale structure to affect long-wavelength tomographic images. If this is the case, geodynamic models should be modified in such a way only, as to reflect the effects of limited resolving power alone.

In this respect, *Mégnin et al.* [1997] have shown that aliasing of short-scale heterogeneity into the low degrees of tomographic models can be observed in the inversion of long period S-wave data for large-scale structure. In other words, velocity variations in the inverted long-wavelength structure may be larger than the actual large-scale structure in Earth due to short-scale structure "seen" by the seismic waves. This implies that the information on short-scale heterogeneity in the seismic data is not totally lost, as for example due to finite frequency effects such as wave front healing, but rather is mapped as additional contribution into the tomographic models. Put differently, the aliasing in tomography

may counteract to some extent the reducing effect of limited tomographic resolution and result in a slight amplification of the long-wavelength anomalies.

The occurrence of structural aliasing is expected from theoretical considerations [*Dahlen*, 2004]: In the case of perfect illumination of a given velocity perturbation by waves with finite frequency, the anomaly recovered with ray-tomography will have the same volume-integrated total perturbation. The recovered anomaly, however, will be broader due to lateral smearing and will have a smaller maximum amplitude. This "mass conservation" of seismic anomalies suggests that only uneven data coverage and the associated need to damp inversions are the reason for tomographically resolved amplitudes being on average (in a root-mean-square sense) smaller than in the Earth.

As for the geodynamic models, the volume-integral of the velocity perturbations is not conserved during reparameterization and we have therefore attempted to correct for the associated magnitude reduction. Taking advantage of the linearity of the resolution operator, it is possible to consider the short-scale structure lost in the long-wavelength parameterization as additional contribution in the statistical characteristics of the tomographically filtered MCMs (see sections 3.5–3.7). This way, an approximation of the magnitude reduction of seismic heterogeneity due to the limited tomographic resolving power alone is provided.

After correcting for reparameterization induced changes in the characteristics of our tomographically filtered geodynamic models, we find that shear wave velocity anomalies are reduced by a factor of around 2 in the bottom 500 km of the mantle (i.e., from the tomographic filtering alone). More specifically, large negative anomalies of -3 to -4% in the lowermost mantle, corresponding to plume excess temperatures of $+1000$–1500 K,

would be mapped as -1.5 to -2%, and are therefore in good agreement with the values of S20RTS. We note that large lateral temperature variations in the lower mantle can be anticipated from a number of geodynamic considerations on plume excess temperatures, including the adiabatic ascent of plumes in the subadiabatic mantle [*Bunge*, 2005] and the fact that the adiabatic gradient is itself temperature dependent, getting steeper with increasing temperature [e.g., *Piazzoni et al.*, 2007].

The corrected histogram of our strongly bottom heated model M2 shows slightly larger maximum velocity anomalies than S20RTS, especially for positive values (compare Figs. 7b and 7c). This may show that accounting for the total amplitude reduction of the reparameterization overestimates the aliasing effect in tomography. In fact, it is likely that the actual structure that should be compared with the tomographic model lies somewhere between models M2^f and M2^{f+}. In this case, the temperature variations may not fully account for the seismic anomalies seen in S20RTS. However, as mentioned in section 2, the mineralogical model used here does not incorporate the effects of anelasticity on seismic velocities. Including these effects would result in a higher sensitivity of v_s to temperature by up to 20–30% compared to the purely elastic case [e.g., *Goes et al.*, 2004; *Brodholt et al.*, 2007]. Thus, in the more realistic case of anelasticity, the thermal anomalies in M2 are still likely to explain most of the seismic signal in the large low velocity zones even if no structural aliasing was present in tomographic inversions (compare M2^f in Fig. 3f with S20RTS in Fig. 7c).

We do not preclude compositional variations in Earth's mantle, but the tomographic filtering of our MCMs shows that it is quite possible to explain seismic heterogeneity by temperature variations alone. This finding may place limits on the potential role of

chemical heterogeneity, as the large plume temperatures anticipated in the lower mantle already account for the seismic signal in the large low velocity zones. An increase in the iron content, for example, added on to the large thermal anomalies, is expected to further enhance the seismic anomalies [*Wang and Weidner*, 1996; *Jackson*, 1998] and will therefore possibly overpredict the magnitudes of velocity variations. Thus, our study lends further support to the notion that global mantle circulation is predominantly thermally driven and has a strong core heating component.

4.2. Horizontal Gradients of Thermal and Seismic Heterogeneity

Sharp horizontal gradients in seismic velocities have sometimes been advanced as an argument for chemical variations [*Ni et al.*, 2002; *Brodholt et al.*, 2007]. Evidence for strong gradients in shear wave velocity, which may be related to anomalously warm buoyant mantle due to continental insulation [*Anderson*, 1982; *Phillips and Bunge*, 2005], comes from the observation of rapid variations of body wave traveltimes over a small azimuthal range for ray-paths turning in the deep mantle under Africa [e.g., *Ritsema et al.*, 1998]. Based on this direct observation, *Ni et al.* [2002] estimated that shear wave velocities in the lower mantle vary by up to 3% over a distance of 50 km (i.e., a gradient of relative perturbations of $\sim 6 \times 10^{-7}\,\mathrm{m}^{-1}$).

To investigate the abruptness with which velocity variations change laterally in isochemical whole mantle flow, we can directly examine our unfiltered models, as we do not need to account for tomographic resolution effects in the comparison to the direct observation of rapid azimuthal traveltime variations.

Our unfiltered MCM M2^o (Fig. 1a) shows slow anomalies in the lowermost mantle directly bounded by fast material. The resulting gradients are around $4.5 \times 10^{-7}\,\mathrm{m}^{-1}$ or

2.25% over 50 km, comparable to the values suggested by *Ni et al.* [2002]. These gradients in shear wave velocity relate to thermal gradients of ~ 0.015–$0.018\,\mathrm{K\,m^{-1}}$ or around 750–900 K per 50 km. Such strong thermal variations in isochemical mantle circulation models are entirely expected, as heat transport inside the Earth is dominated by advection (typical Peclet numbers of around 10–100) so that sharp gradients are preserved.

4.3. Current Limitations in the Comparison of Geodynamic and Tomographic Seismic Heterogeneity

In the present study, we concentrated on variations in shear wave velocity and the comparison to S20RTS. It would be helpful to also compare our MCMs to other tomographic S-wave models, as well as to compare the additionally predicted v_p heterogeneity to tomographic P-wave models. However, resolution matrices are currently available for only a few tomographic models. In fact, for models with a large number of parameters in the inversion, the construction of $\mathcal{R}$ is computationally not feasible [Nolet, 2008; pers. comm.]. A further complication arises from the varying degrees of approximations concerning the forward problem of seismology used in different tomographic studies. Furthermore, direct comparison of S- and P-wave models may be biased due to the different frequency content of the respective data sets. The approach taken here thus seems currently not well suited to address the question of potential anticorrelation of v_s with bulk sound velocity v_ϕ, or density, in the lowermost mantle.

With respect to structural aliasing in tomographic inversions, further studies are needed to better quantify the extent to which this is affecting the long-wavelength tomographic images. It also remains to be seen whether the rise of multi-frequency traveltime and amplitude tomography [*Sigloch and Nolet*, 2006; *Sigloch et al.*, 2008], or alternatively

inversions based on the adjoint method [e.g., *Fichtner et al.*, 2006a, b], will result in better resolution of the geometry, amplitude and especially the gradients of seismic heterogeneity.

Our conclusions are furthermore limited in that the mineralogical models currently do not include the post-perovskite phase. Recent studies point to the possibility that the anticorrelation of lower mantle shear and bulk sound velocity variations may be caused by phase heterogeneity associated with post-perovskite [*Hutko et al.*, 2008; *Hernlund and Houser*, 2008]. However, post-perovskite is likely to occur only in cold regions of the lowermost mantle [*Tateno et al.*, 2009] and therefore our results on high plume excess temperatures will probably not be affected much.

5. Conclusions

We have quantitatively related lateral temperature variations to magnitudes of seismic heterogeneity taking into account their complex relation through mantle mineralogy and the effects of limited tomographic resolution. In our analysis, we concentrated on isochemical whole mantle circulation to study the effects of bottom heating without any complications due to compositional variations. We have focused on models with strong core heating, as a number of studies have argued for a large thermal gradient across D″ on the order of 1000 K and a high core heat flow.

The tomographic filtering of seismic velocity structures involves the reparameterization of our geodynamic models onto the long-wavelength basis of S20RTS. The drastic decrease in model dimensionality from 8×10^7 to 10^4 results in an artificial reduction of the magnitude of seismic heterogeneity. Based on the linearity of the resolution operator, we have shown that the short-scale heterogeneity lost in the reparameterization can be considered as an additional contribution to the statistical characteristics of the filtered MCMs.

With this correction, we arrive at a consistent comparison with tomography, as it is likely that seismic inversions inherently incorporate information on short-scale variations due to structural aliasing.

We find a good agreement of the tomographically filtered and reparameterization corrected MCMs with S20RTS. However, only the MCM with strong core heating shows magnitudes of slow seismic anomalies in the lowermost mantle that are compatible with the values seen in S20RTS. Shear wave velocity perturbations of -3 to -4% in this model are reduced by a factor of 2 when accounting for uneven data coverage and damping. Furthermore, thermal gradients of around 750–900 K per 50 km in the corresponding unfiltered model result in shear wave velocity gradients of $\sim 2.25\%$ over 50 km, which are in good agreement with the study of *Ni et al.* [2002] for the sharp sides of the African superplume. Our results thus confirm the conclusion of *Schuberth et al.* [2009] that isochemical whole mantle circulation with substantial CMB heat flow of 9–12 TW and a pyrolite composition is consistent with a number of seismic observations on the lower mantle.

References

Alfè, D., G. D. Price, and M. J. Gillan (2002), Iron under Earth's core conditions: Liquid-state thermodynamics and high-pressure melting curve from ab initio calculations, *Physical Review B*, *65*(16), 165,118–165,129, doi:10.1103/PhysRevB.65.165118.

Alfè, D., M. J. Gillan, and G. D. Price (2007), Temperature and composition of the Earth's core, *Contemporary Physics*, *48*(2), 63–80, doi:10.1080/00107510701529653.

Anderson, D. L. (1982), Hotspots, polar wander, Mesozoic convection and the geoid, *Nature*, *297*(5865), 391–393.

Becker, T. W., and R. J. O'Connell (2001), Predicting plate velocities with mantle circulation models, *Geochem. Geophys. Geosyst.*, *2*(12), doi:10.1029/2001GC000171, 2001.

Boehler, R. (2000), High-pressure experiments and the phase diagram of lower mantle and core materials, *Rev. Geophys.*, *38*(2), 221–245.

Brodholt, J. P., G. Helffrich, and J. Trampert (2007), Chemical versus thermal heterogeneity in the lower mantle: The most likely role of anelasticity, *Earth Planet. Sci. Lett.*, *262*(3-4), 429–437, doi:10.1016/j.epsl.2007.07.054.

Buffett, B. A. (2002), Estimates of heat flow in the deep mantle based on the power requirements for the geodynamo, *Geophys. Res. Lett.*, *29*(12), 1566, doi:10.1029/2001GL014649.

Bunge, H. P. (2005), Low plume excess temperature and high core heat flux inferred from non-adiabatic geotherms in internally heated mantle circulation models, *Phys. Earth*

Planet. Inter., *153*(1-3), 3–10, doi:10.1016/j.pepi.2005.03.017.

Bunge, H. P., and J. H. Davies (2001), Tomographic images of a mantle circulation model, *Geophys. Res. Lett.*, *28*(1), 77–80.

Bunge, H.-P., and M. Richards (1996), The origin of large-scale structure in mantle convection: Effects of plate motions and viscosity stratification, *Geophys. Res. Lett.*, *23*, 2987–2990.

Bunge, H.-P., M. Richards, and J. Baumgardner (1996), The effect of depth-dependent viscosity on the planform of mantle convection, *Nature*, *379*, 436–438, doi: 10.1038/379436a0.

Bunge, H.-P., M. Richards, and J. Baumgardner (1997), A sensitivity study of 3D-spherical mantle convection at 10exp8 rayleigh number: effects of depth-dependent viscosity, heating mode and an endothermic phase change, *J. Geophys. Res.*, *102*, 11,991–12,007.

Bunge, H.-P., M. Richards, C. Lithgow-Bertelloni, J. Baumgardner, S. Grand, and B. Romanowicz (1998), Time scales and heterogeneous structure in geodynamic Earth models, *Science*, *280*, 91–95, doi:10.1126/science.280.5360.91.

Bunge, H.-P., M. Richards, and J. Baumgardner (2002), Mantle circulation models with sequential data-assimilation: Inferring present-day mantle structure from plate motion histories, *Phil. Trans. Roy. Soc. A*, *360*(1800), 2545–2567, doi:10.1098/rsta.2002.1080.

Bunge, H.-P., C. R. Hagelberg, and B. J. Travis (2003), Mantle circulation models with variational data-assimilation: Inferring past mantle flow and structure from plate motion histories and seismic tomography, *Geophys. J. Int.*, *2*(152), 280–301, doi: 10.1046/j.1365-246X.2003.01823.x.

Conrad, C. P., and C. Lithgow-Bertelloni (2002), How mantle slabs drive plate tectonics, *Science*, *298*(5591), 207–209, doi:10.1126/science.1074161.

Dahlen, F. A. (2004), Resolution limit of traveltime tomography, *Geophys. J. Int.*, *157*(1), 315–331, doi:10.1111/j.1365-246X.2004.02214.x.

Dahlen, F. A., and J. Tromp (1998), *Theoretical Global Seismology*, Princeton University Press, Princeton, New Jersey.

Davies, J. H., and H. P. Bunge (2001), Seismically "fast" geodynamic mantle models, *Geophys. Res. Lett.*, *28*(1), 73–76.

Dziewonski, A. M., and D. L. Anderson (1981), Preliminary reference Earth model, *Phys. Earth Planet. Inter.*, *25*, 297–356, doi:10.1016/0031-9201(81)90046-7.

Dziewonski, A. M., B. H. Hager, and R. J. O'Connell (1977), Large-Scale Heterogeneities in the Lower Mantle, *J. Geophys. Res.*, *82*(2), 239–255.

Farnetani, C. G., and H. Samuel (2005), Beyond the thermal plume paradigm, *Geophys. Res. Lett.*, *32*(7), L07,311, doi:10.1029/2005GL022360.

Fichtner, A., H.-P. Bunge, and H. Igel (2006a), The adjoint method in seismology: I - Theory, *Phys. Earth Planet. Inter.*, *157*(1-2), 86–104, doi:10.1016/j.pepi.2006.03.016.

Fichtner, A., P. Bunge, and H. Igel (2006b), The adjoint method in seismology: II - Applications: traveltimes and sensitivity functionals, *Phys. Earth Planet. Inter.*, *157*(1-2), 105–123, doi:10.1016/j.pepi.2006.03.018.

Glatzmaier, G. A., and P. H. Roberts (1995), A 3-dimensional self-consistent computer-simulation of a geomagnetic-field reversal, *Nature*, *377*(6546), 203–209, doi:10.1038/377203a0.

Goes, S., F. Cammarano, and U. Hansen (2004), Synthetic seismic signature of thermal mantle plumes, *Earth Planet. Sci. Lett.*, *218*(3-4), 403–419, doi:10.1016/S0012-821X(03)00680-0.

Grand, S., R. van der Hilst, and S. Widiyantoro (1997), Global seismic tomography: A snapshot of mantle convection in the Earth, *GSA Today*, *7*, 1–7.

Gubbins, D., D. Alfe, G. Masters, G. D. Price, and M. Gillan (2004), Gross thermodynamics of two-component core convection, *Geophys. J. Int.*, *157*(3), 1407–1414, doi: 10.1111/j.1365-246X.2004.02219.x.

Hernlund, J. W., and C. Houser (2008), On the statistical distribution of seismic velocities in Earth's deep mantle, *Earth Planet. Sci. Lett.*, *265*(3-4), 423–437, doi: 10.1016/j.epsl.2007.10.042.

Houser, C., G. Masters, P. Shearer, and G. Laske (2008), Shear and compressional velocity models of the mantle from cluster analysis of long-period waveforms, *Geophys. J. Int.*, *174*(1), 195–212, doi:10.1111/j.1365-246X.2008.03763.x.

Hutko, A. R., T. Lay, J. Revenaugh, and E. J. Garnero (2008), Anticorrelated seismic velocity anomalies from post-perovskite in the lowermost mantle, *Science*, *320*(5879), 1070–1074, doi:10.1126/science.1155822.

Ishii, M., and J. Tromp (2001), Even-degree lateral variations in the Earth's mantle constrained by free oscillations and the free-air gravity anomaly, *Geophys. J. Int.*, *145*(1), 77–96, doi:10.1111/j.1365-246X.2001.00385.x.

Jackson, I. (Ed.) (1998), *The Earth's Mantle*, Cambridge University Press, — Sig.: Bf161.

Jordan, T. H., P. Puster, G. A. Glatzmaier, and P. J. Tackley (1993), Comparisons between seismic Earth structures and mantle flow models based on radial correlation-

functions, *Science*, *261*(5127), 1427–1431, doi:10.1126/science.261.5127.1427.

Kennett, B. L. N., S. Widiyantoro, and R. D. van der Hilst (1998), Joint seismic tomography for bulk sound and shear wave speed in the Earth's mantle, *J. Geophys. Res.*, *103*(B6), 12,469–12,493.

Kuang, W. L., and J. Bloxham (1997), An earth-like numerical dynamo model, *Nature*, *389*(6649), 371–374, doi:10.1038/38712.

Kustowski, B., G. Ekstrom, and A. M. Dziewonski (2008), Anisotropic shear-wave velocity structure of the Earth's mantle: A global model, *J. Geophys. Res.*, *113*(B6), B06,306.

Li, X. D., and B. Romanowicz (1995), Comparison of global wave-form inversions with and without considering cross-branch modal coupling, *Geophys. J. Int.*, *121*(3), 695–709.

Li, X. D., and B. Romanowicz (1996), Global mantle shear velocity model developed using nonlinear asymptotic coupling theory, *J. Geophys. Res.*, *101*(B10), 22,245–22,272.

Lithgow-Bertelloni, C., and M. A. Richards (1998), The dynamics of Cenozoic and Mesozoic plate motions, *Rev. Geophys.*, *36*(1), 27–78.

Masters, G., G. Laske, H. Bolton, and A. M. Dziewonski (2000), *Earth's Deep Interior – Mineral Physics and Tomography From the Atomic to the Global Scale*, chap. The Relative Behavior of Shear Velocity, Bulk Sound Speed, and Compressional Velocity in the Mantle: Implications for Chemical and Thermal Structure, pp. 63–87, American Geophysical Union, Washington D.C.

McNamara, A., and S. Zhong (2005), Thermochemical structures beneath Africa and the Pacific Ocean, *Nature*, *437*, 1136–1139, doi:10.1038/nature04066.

McNamara, A. K., and S. J. Zhong (2004), The influence of thermochemical convection on the fixity of mantle plumes, *Earth Planet. Sci. Lett.*, *222*(2), 485–500, doi:

10.1016/j.epsl.2004.03.008.

McNamara, A. K., P. E. van Keken, and S. I. Karato (2002), Development of anisotropic structure in the Earth's lower mantle by solid-state convection, *Nature*, *416*(6878), 310–314, doi:10.1038/416310a.

Mégnin, C., H.-P. Bunge, B. Romanowicz, and M. Richards (1997), Imaging 3-D spherical convection models: What can seismic tomography tell us about mantle dynamics?, *Geophys. Res. Lett.*, *24*(11), 1299–1302, doi:10.1029/97GL01256.

Montelli, R., G. Nolet, F. A. Dahlen, and G. Masters (2006), A catalogue of deep mantle plumes: New results from finite-frequency tomography, *Geochem. Geophys. Geosyst.*, *7*, Q11,007, doi:10.1029/2006GC001248.

Ni, S. D., E. Tan, M. Gurnis, and D. V. Helmberger (2002), Sharp sides to the African superplume, *Science*, *296*, 1850–1852, doi:10.1126/science.1070698.

Nimmo, F., G. D. Price, J. Brodholt, and D. Gubbins (2004), The influence of potassium on core and geodynamo evolution, *Geophys. J. Int.*, *156*(2), 363–376, doi: 10.1111/j.1365-246X.2003.02157.x.

Nolet, G., S. I. Karato, and R. Montelli (2006), Plume fluxes from seismic tomography, *Earth Planet. Sci. Lett.*, *248*, 685–699, doi:10.1016/j.epsl.2006.06.011.

Oeser, J., H. P. Bunge, and M. Mohr (2006), Cluster design in the earth sciences - Tethys, *High Performance Computing And Communications, Proceedings*, *4208*, 31–40.

Panning, M., and B. Romanowicz (2006), A three dimensional radially anisotropic model of shear velocity in the whole mantle, *Geophys. J. Int.*, *167*, 361–379.

Phillips, B. R., and H.-P. Bunge (2005), Heterogeneity and time dependence in 3D spherical mantle convection models with continental drift, *Earth Planet. Sci. Lett.*, *233*(1-2),

121–135, doi:10.1016/j.epsl.2005.01.041.

Piazzoni, A. S., G. Steinle-Neumann, H.-P. Bunge, and D. Dolejš (2007), A mineralogical model for density and elasticity of the Earth's mantle, *Geochem. Geophys. Geosyst.*, *8*, doi:10.1029/2007GC001697.

Richards, M. A., and D. C. Engebretson (1992), Large-scale mantle convection and the history of subduction, *Nature*, *355*(6359), 437–440, doi:10.1038/355437a0.

Ritsema, J., and H. J. van Heijst (2001), Constraints on the correlation of P- and S-wave velocity heterogeneity in the mantle from P, PP, PPP, and PKPab traveltimes, *Geophys. J. Int.*, *149*(2), 483–490.

Ritsema, J., and H. J. van Heijst (2002), Constraints on the correlation of P- and S-wave velocity heterogeneity in the mantle from P, PP, PPP and PKPab traveltimes, *Geophys. J. Int.*, *149*(2), 482–489, doi:10.1046/j.1365-246X.2002.01631.x.

Ritsema, J., S. Ni, D. V. Helmberger, and H. P. Crotwell (1998), Evidence for Strong Shear Velocity Reductions and Velocity Gradients in the Lower Mantle Beneath Africa, *Geophys. Res. Lett.*, *25*(23), 4245–4248.

Ritsema, J., H. J. van Heijst, and J. H. Woodhouse (2004), Global transition zone tomography, *J. Geophys. Res.*, *109*(B2), doi:10.1029/2003JB002610.

Ritsema, J., A. K. McNamara, and A. L. Bull (2007), Tomographic filtering of geodynamic models: Implications for model interpretation and large-scale mantle structure, *J. Geophys. Res.*, *112*(B1), B01,303, doi:10.1029/2006JB004566.

Robertson, G. S., and J. H. Woodhouse (1995), Evidence for proportionality of p and s heterogeneity in the lower mantle, *Geophys. J. Int.*, *123*(1), 85–116.

Samuel, H., C. G. Farnetani, and D. Andrault (2005), *Earth's Deep Mantle: Structure, Composition, and Evolution*, chap. Heterogeneous lowermost mantle: Compositional constraints and seismological observables, pp. 101–116, AGU.

Schuberth, B. S. A., H.-P. Bunge, G. Steinle-Neumann, C. Moder, and J. Oeser (2009), Thermal versus elastic heterogeneity in high-resolution mantle circulation models with pyrolite composition: High plume excess temperatures in the lowermost mantle, *Geochem. Geophys. Geosyst.*, *10*(1), Q01W01, doi:10.1029/2008GC002235.

Sigloch, K., and G. Nolet (2006), Measuring finite-frequency body-wave amplitudes and traveltimes, *Geophys. J. Int.*, *167*(1), 271–287.

Sigloch, K., N. McQuarrie, and G. Nolet (2008), Two-stage subduction history under North America inferred from multiple-frequency tomography, *Nature Geoscience*, *1*(7), 458–462, doi:10.1038/ngeo231.

Simmons, N. A., A. M. Forte, and S. P. Grand (2007), Thermochemical structure and dynamics of the African superplume, *Geophys. Res. Lett.*, *34*, L02,301, doi: 10.1029/2006GL028009.

Steinberger, B., and R. Holme (2008), Mantle flow models with core-mantle boundary constraints and chemical heterogeneities in the lowermost mantle, *J. Geophys. Res.*, *113*(B5), B05,403, doi:10.1029/2007JB005080.

Steinle-Neumann, G., L. Stixrude, R. E. Cohen, and O. Gulseren (2001), Elasticity of iron at the temperature of the Earth's inner core, *Nature*, *413*(6851), 57–60, doi: 10.1038/35092536.

Stixrude, L., and C. Lithgow-Bertelloni (2005), Thermodynamics of mantle minerals - I. Physical properties, *Geophys. J. Int.*, *162*(2), 610–632, doi:10.1111/j.1365-

246X.2005.02642.x.

Stixrude, L., and C. Lithgow-Bertelloni (2007), Influence of phase transformations on lateral heterogeneity and dynamics in earth's mantle, *Earth Planet. Sci. Lett.*, *263*, 45–55, doi:10.1016/j.epsl.2007.08.027.

Su, W.-j., and A. M. Dziewonski (1997), Simultaneous inversion for 3-D variations in shear and bulk velocity in the mantle, *Phys. Earth Planet. Inter.*, *100*(1-4), 135–156, doi:10.1016/S0031-9201(96)03236-0.

Su, W.-j., R. L. Woodward, and A. M. Dziewonski (1994), Degree 12 model of shear velocity heterogeneity in the mantle, *J. Geophys. Res.*, *99*(B4), 6945–6980.

Tateno, S., K. Hirose, N. Sata, and Y. Ohishi (2009), Determination of post-perovskite phase transition boundary up to 4400 k and implications for thermal structure in D'' layer, *Earth Planet. Sci. Lett.*, *277*(1-2), 130 – 136, doi:10.1016/j.epsl.2008.10.004.

Trampert, J., F. Deschamps, J. Resovsky, and D. Yuen (2004), Probabilistic tomography maps chemical heterogeneities throughout the lower mantle, *Science*, *306*(5697), 853–856, doi:10.1126/science.1101996.

van der Hilst, R. D., and H. Karason (1999), Compositional heterogeneity in the bottom 1000 kilometers of earth's mantle: Toward a hybrid convection model, *Science*, *283*(5409), 1885–1888, doi:10.1126/science.283.5409.1885.

van der Hilst, R. D., S. Widiyantoro, and E. R. Engdahl (1997), Evidence for deep mantle circulation from global tomography, *Nature*, *386*(6625), 578–584, doi:10.1038/386578a0.

van der Hilst, R. D., M. V. de Hoop, P. Wang, S. H. Shim, P. Ma, and L. Tenorio (2007), Seismostratigraphy and thermal structure of Earth's core-mantle boundary region, *Science*, *315*, 1813–1817, doi:10.1126/science.1137867.

Wang, Y., and L. Wen (2004), Mapping the geometry and geographic distribution of a very low velocity province at the base of the Earth's mantle, *J. Geophys. Res.*, *109*(B10), B10,305, doi:10.1029/2003JB002674.

Wang, Y. B., and D. J. Weidner (1996), $(\frac{\partial \mu}{\partial T})_P$ of the lower mantle, *Pure Appl. Geophys.*, *146*(3-4), 533–549, doi:10.1007/BF00874732.

Wen, L. X., P. G. Silver, D. James, and R. Kuehnel (2001), Seismic evidence for a thermo-chemical boundary at the base of the Earth's mantle, *Earth Planet. Sci. Lett.*, *189*, 141–153, doi:10.1016/S0012-821X(01)00365-X.

Wessel, P., and W. H. F. Smith (1991), Free software helps map and display data, *EOS Trans. AGU*, *72*(441), 441.

Figure 1. Depth slices through (a–c) mantle circulation model M2 (35% core heating) and (d) tomographic model S20RTS [*Ritsema et al.*, 2004]. Variations in S-wave velocity are given relative to the corresponding radial average profile in case of M2, and relative to PREM [*Dziewonski and Anderson*, 1981] in the case of S20RTS. (a) M2 in the original parameterization of the code TERRA (around 80 million grid points resulting in ∼25 km global grid spacing) [*Schuberth et al.*, 2009]. (b) M2 in the parameterization of S20RTS (spherical harmonics up to degree 20 and 21 radial splines resulting in ∼10,000 model parameters and a spatial resolution on the order of 1000 km). Note the reduction of the magnitudes of seismic heterogeneity introduced by the reparameterization. (c) M2 after tomographic filtering; that is, the reparameterized model multiplied with the resolution operator of S20RTS so that it reflects the limited resolving power due to uneven data coverage and damping. A further reduction of heterogeneity can be observed, as well as lateral smearing of structure. See section 2 for details on the different parameterizations and the tomographic filtering.

Figure 2. Spectral heterogeneity maps (SHM) for mantle circulation models M1 and M2. The spectral power of relative variations in v_s is given on a logarithmic color scale and plotted as a function of spherical harmonic degree and depth. Small sub-plots on the right of each spectral heterogeneity map show the root-mean-square power up to degree 20. (a–c) SHMs for M1 (5% core heating) in (a) the original parameterization, (b) the parameterization of S20RTS and (c) after tomographic filtering. (d–f) SHMs for M2 (35% core heating), accordingly.
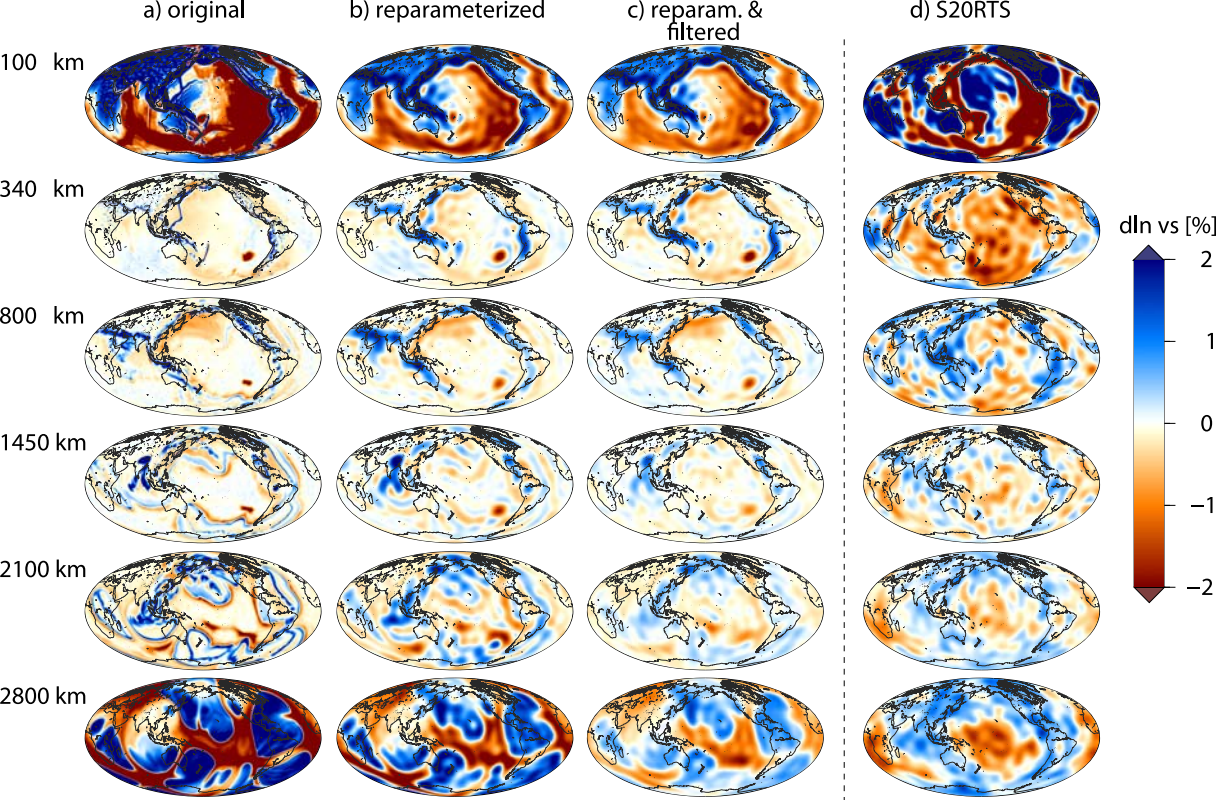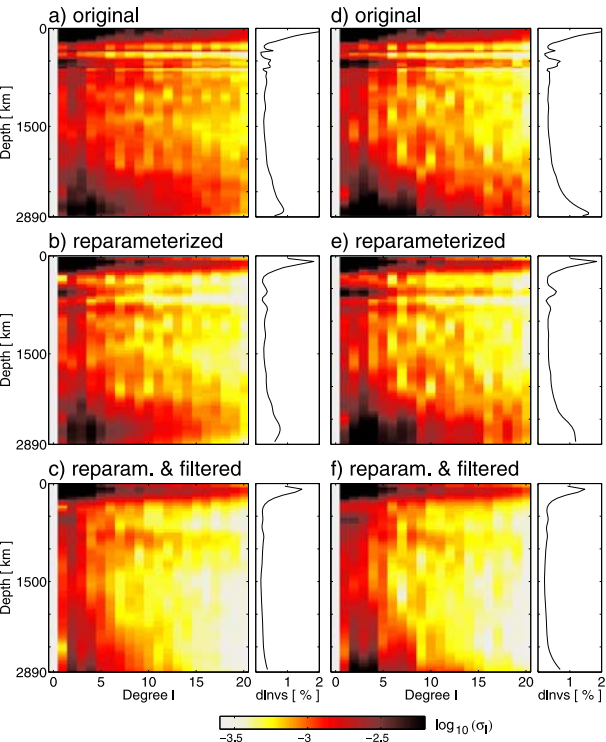
Figure 3. Histograms of relative variations in v_s for mantle circulation models M1 and M2. Logarithmic color scale and contours represent the total number of model grid points (ngp) at any given depth (y-axis) as a function of their shear wave anomaly relative to the horizontal mean (x-axis). Contour lines are plotted for $log_{10}(ngp) = 1, 2, 3, 3.8$ and 4.2. The histograms are normalized to the number of grid points in the original parameterization of our models to allow for a direct comparison. This is done by scaling the distributions obtained from the models in the S20RTS parameterization by the ratio $\frac{ngp^o}{ngp^r}$. (a–c) Histograms for M1 (5% core heating) in (a) the original parameterization, (b) the parameterization of S20RTS and (c) after tomographic filtering. (d–f) Histograms for M2 (35% core heating), accordingly.

Figure 4. (a) Root-mean-square amplitudes of heterogeneity in mantle circulation model M2 as a function of depth. RMS profiles of relative variations in v_s are given for M2 in (blue) the original parameterization, (red) the parameterization of S20RTS, and (green) after tomographic filtering. (b) Separated contributions to the total relative amplitude reduction seen in Figure 4a resulting from the combination of reparameterization and tomographic filtering with the resolution matrix $\mathcal{R}$. (cyan) Total relative amplitude reduction between the original and the tomographically filtered model (blue and green line in Figure 4a). (magenta) Relative amplitude reduction due to the reparameterization; that is, between the original and the reparameterized model (blue and red line in Figure 4a). (brown) Relative amplitude reduction due to the tomographic filtering; that is between the reparameterized and the tomographically filtered model (red and green line in Figure 4a). Note that the reparameterization predominantly affects the upper half of the mantle, while the tomographic filtering effects are stronger in the lower half. Taken together, the total amplitude reduction is almost constant with depth in the lower mantle.

Figure 5.   RMS profiles of relative variations in v_s for the tomographically filtered mantle circulation models (red) M1 and (blue) M2 corrected for the effects of reparameterization (see section 3.5 for details on the correction). The RMS profile of S20RTS [*Ritsema et al.*, 2004] is shown for comparison (black dashed line).

Figure 6.   Spectral heterogeneity maps for the tomographically filtered models (a) M1 and (b) M2, corrected for the loss of power introduced by the reparameterization (i.e., M1^{f+} and M2^{f+}). Spectral power of v_s heterogeneity is given on a logarithmic color scale and plotted as a function of spherical harmonic degree and depth. See section 3.6 for details on the correction for the effects of reparameterization. (c) Spectral heterogeneity map for S20RTS [*Ritsema et al.*, 2004].

Figure 7.   Histograms of relative variations in v_s for the tomographically filtered models (a) M1 and (b) M2, corrected for the magnitude reduction resulting from the reparameterization (i.e., M1^{f+} and M2^{f+}). Logarithmic color scale and contours represent the total number of model grid points (ngp) at any given depth (y-axis) as a function of their shear wave anomaly relative to the horizontal mean (x-axis). Contour lines are plotted for $log_{10}(ngp) = 1, 2, 3, 3.8$ and 4.2. See sections 3.7 and 4 for details on the correction for the effects of reparameterization. (c) Histogram for S20RTS [*Ritsema et al.*, 2004]. The histograms are normalized to the number of grid points of the original parameterization of our MCMs to allow for a direct comparison with Figure 3. This is done by scaling the distributions obtained from the models in the S20RTS parameterization by the ratio $\frac{ngp^o}{ngp^r}$. Note the good agreement between M2 and S20RTS for both positive and negative anomalies.
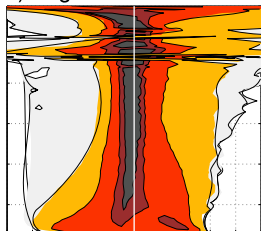
	a) original	b) reparameterized	c) reparam. & filtered	d) S20RTS
100 km				
340 km				
800 km				
1450 km				
2100 km				
2800 km				

dln vs [%]
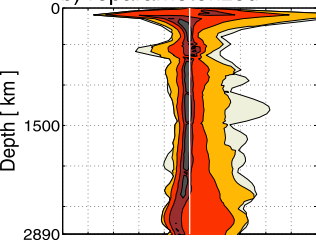
2
1
0
-1
-2

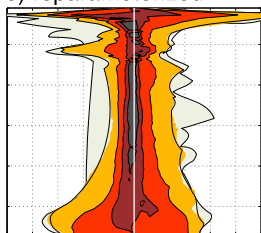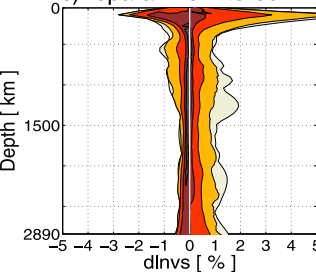**M1: 5% Q_CMB** (Q_{CMB})   **M2: 35% Q_CMB** (Q_{CMB})
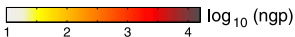
a) original   d) original

b) reparameterized   e) reparameterized

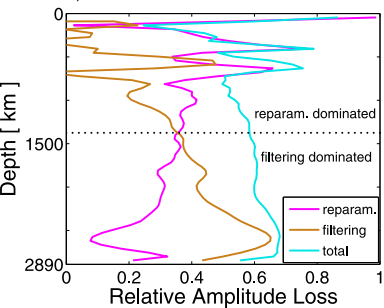c) reparam. & filtered   f) reparam. & filtered

Depth [km]
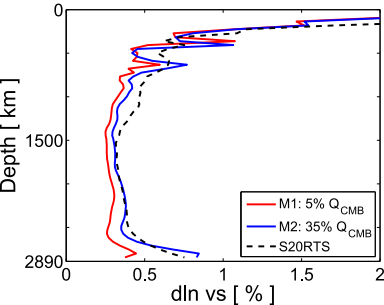
Degree l   dInvs [%]

$\log_{10}(\sigma_l)$

M1: 5% Q_CMB

M2: 35% Q_CMB

a) original
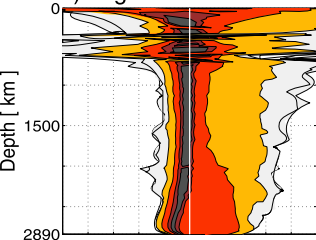
d) original

b) reparameterized

e) reparameterized

c) reparam. & filtered

f) reparam. & filtered

Depth [km]

dlnvs [%]

log_{10} (ngp)
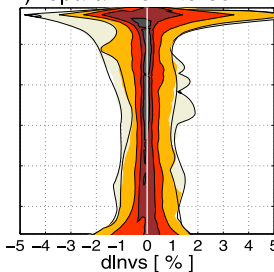
a) RMS amplitudes for M2, 35% Q_{CMB}

- original
- reparameterized
- reparam. & filtered

dln vs [%]

Depth [km]
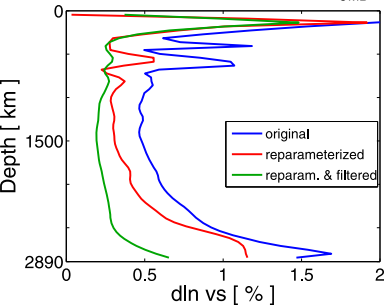
b) Contributions to Reduction of RMS

reparam. dominated

filtering dominated

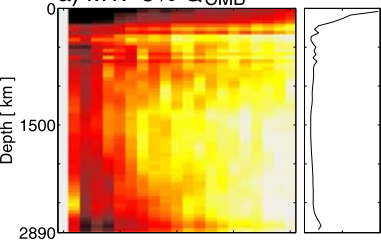- reparam.
- filtering
- total

Relative Amplitude Loss

Depth [km]

RMS corrected for reparameterization

SHMs corrected for reparameterization

a) M1: 5% Q_{CMB}

b) M2: 35% Q_{CMB}

c) S20RTS

Depth [km]

Degree l

dlnvs [%]

$\log_{10}(\sigma_l)$
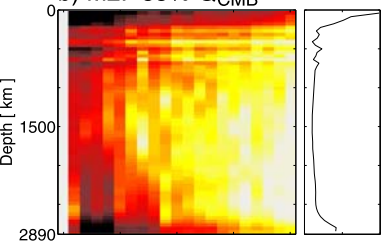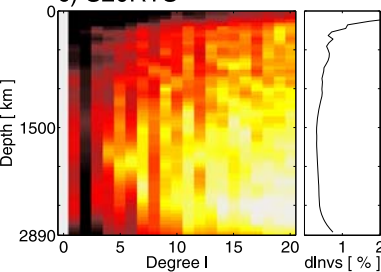
Histograms corrected for reparameterization

a) M1: 5% Q_{CMB}

b) M2: 35% Q_{CMB}

c) S20RTS

$\log_{10}(ngp)$